Quantum lattice effects in mixed-valence transition-metal chain complexes

H. Fehske and M. Kinateder
Physikalisches Institut, Universität Bayreuth, 95440 Bayreuth, Germany

G. Wellein
Regionales Rechenzentrum Erlangen, Universität Erlangen, 91058 Erlangen, Germany

A. R. Bishop
Theoretical Division and Center for Nonlinear Studies, Los Alamos National Laboratory, Los Alamos, New Mexico 87545

(Received 21 December 2000; published 8 June 2001)

Inspired by the recent observation of intrinsically localized vibrational modes in halide-bridged transition-metal chain complexes [Swanson *et al.* Phys. Rev. Lett. **82**, 3288 (1999)], we study strong-coupling effects between electronic and lattice degrees of freedom on the basis of a two-band, 3/4-filled Peierls-Hubbard model. Combining a very efficient Jacobi-Davidson algorithm with the maximum entropy method, the low-energy physics of the Peierls-Hubbard model is analyzed in finite chains with high accuracy, preserving the full dynamics of the Raman- and infrared-active phonon modes. Results for several experimental observables, including the valence disproportionation, local magnetic moments, lattice distortions, spin and charge structure factors, and optical response are discussed. The redshift of the overtone resonance Raman spectrum is calculated to be in quantitative agreement with the experimental data found for isotopically pure $Pt^{37}Cl$. Most significantly, the numerical results provide clear evidence of the existence of spatially localized multiphonon bound states in quasi-one-dimensional charge-density-wave systems with strong electron-lattice coupling.

DOI: 10.1103/PhysRevB.63.245121 PACS number(s): 71.10.−w, 71.38.−k, 71.28.+d, 63.22.+m

I. INTRODUCTION

Quasi-one-dimensional MX solids, consisting of chains of transition-metal ions (M=Pt, Pd, Ni) bridged by halogens (X=Cl, Br, I), have been the subject of intense experimental and theoretical study because the various compounds of the family exhibit a remarkable range of strengths of competing electron-electron γ and electron-lattice forces, and consequent physical properties.[1–5] Most notably, these systems exhibit a wide variety of broken-symmetry ground states, ranging from a charge-density wave (CDW) in platinum based materials to a spin-density wave (SDW) in nickel-based materials.[6] A particularly interesting class are the PtX compounds, which are typically Peierls distorted, where the charge disproportionation (alternating valence) of the Ms sublattice is stabilized by a structural distortion of the X sublattice (see Fig. 1). The degree of the Peierls distortion can be varied, e.g., by changing the halide, with PtCl, PtBr, and PtI typical of MX chains ranging from strongly to weakly distorted limits. Because of the tunability of the strength of the CDW, the size of the energy gap between the occupied and unoccupied states can also be varied over a strikingly large range. This has important consequences for the spatial configuration of gap states created by inhomogeneities or local defects in the process of structural relaxation. These gap states can be charged, such as electron-hole polarons and bipolarons, or neutral, such as (photoexcited) excitons. In all cases, they are accompanied by a *local* lattice distortion ranging in size from one or two unit cells in PtCl to more then 30 unit cells in PtI. If the lattice distortion is large and highly localized, the energies of the gap states are relatively far from the valence- and conducting-band edges. Then those multiphonon gap states are tightly bound and can diffuse along the chain only by (incoherent) quantum mechanically hopping processes. Consequently the vibrational energy is localized in a small segment of the MX chain near the imperfection.

In this context, a question of principle arises as to whether, in addition to this familiar disorder-induced localization of vibrational energy, a dynamical, *intrinsic* localization of phonons might take place in *pure* MX solids. Theoretically, such intrinsically localized vibrational modes (ILM's) have been postulated to occur in an extended periodic lattice when both *nonlinearity* (anharmonicity) and *discreteness* are present with sufficient strengths.[7] From this point of view, the highly discrete crystalline, strong-CDW MX materials seem to be good candidates and indeed, very recently, an experimental observation of ILM's has been reported in $[Pt(en)_2][Pt(en)_2Cl_2](ClO_4)_4$ (en-ethylenediamine),[8] subsequently denoted by PtCl. In isotopically pure PtCl the source of the nonlinearity is the strong coupling between electronic and lattice degrees of freedom,

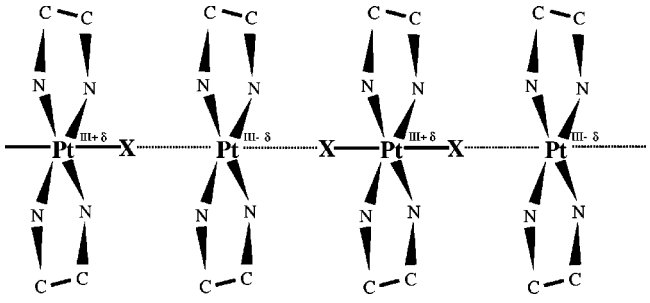

FIG. 1. Basic structure of the $[Pt(en)_2][Pt(en)_2X_2](ClO_4)_4$ chain material [not shown, for clarity, are the H atoms of the (en) ligands and the ClO_4^- counter ions (after Ref. 4)].

and consequently resonance Raman spectroscopy has been used as an ideal experimental technique to measure the energy of the characteristic lattice vibrations associated with the local distortions of the gap states. The ILM's are identified by the strong redshifts they impose upon the overtone resonance Raman spectra. A first theoretical modeling of the observed redshift was based on a nonadiabatic coupled electron-lattice Hamiltonian for a single Pt_2Cl_2 unit.[8,9]

In this paper we use an exact numerical approach based on the Jacobi-Davidson and maximum entropy methods in order to investigate the ground-state and spectral properties of the two-band Hubbard model coupled to both Raman- and infrared-active phonon modes without any adiabatic approximation and for significant chain lengths. Calculating the redshift of the resonance Raman spectra, we confirm the existence of ILM's in the coupled electron-phonon system considered. Clear signatures of these localized multiphonon bound states are also found in the optical response.

The paper is organized as follows: In Sec. II we introduce the Peierls-Hubbard Hamiltonian and comment on the model parameters appropriate for PtCl. In Sec. III we analyze the ground-state properties of the Peierls-Hubbard model. Section IV presents exact diagonalization results for the excitations; in particular, we calculate the optical conductivity and discuss the occurrence of ILM's, using chains of eight sites in length.[10] Our main conclusions are summarized in Sec. V. The work is supplemented by two appendices illustrating the technical details of the computational procedures such as the implementation of the electron-phonon basis (Appendix A) and the efficiency and accuracy of the Jacobi-Davidson algorithm compared to the standard Lanczos diagonalization technique (Appendix B).

II. MODEL

The MX materials constitute a 3/4-filled, two-band electronic system if one takes into account a single orbital per ion (the M d_z^2 and X p_z^2 orbitals with six electrons per M_2X_2 unit cell at stoichiometry).[11] Including only nearest-neighbor (NN) hopping processes between adjacent metal and halide sites, our starting point is the one-dimensional two-band tight-binding Hubbard model

$$\mathcal{H}_{\rm el}=\sum_{l\alpha\sigma}\varepsilon_\alpha n_{l\alpha\sigma}-t\sum_{\langle l\alpha,l'\alpha'\rangle\sigma}c^\dagger_{l\alpha\sigma}c_{l'\alpha'\sigma}+\sum_{l\alpha}U_\alpha n_{l\alpha\uparrow}n_{l\alpha\downarrow}, \tag{1}$$

where $c^\dagger_{l\alpha\sigma}$ ($c_{l\alpha\sigma}$) creates (annihilates) an electron with spin projection σ in a Wannier state at site $\{l,\alpha\}$, and $n_{l\alpha\sigma}$ is the corresponding fermion number operator. Here l and l' label the unit cells, and we use the convention that the M (X) atoms sit on even (odd) sites denoted by the intracell index $\alpha,\alpha'=2,4$ (1,3). Their on-site energies ε_α can be parametrized by the difference between metal and halogen electron affinities $\Delta=\varepsilon_M-\varepsilon_X$. The other parameters of model (1) are the NN transfer amplitude t and the on-site (Hubbard) electron-electron interactions U_α.[12]

Discussing the lattice degrees of freedom, we consider only the one-dimensional (Peierls distorted) $[\text{—}X\text{-}M^{(III+\delta)}\text{-}X\text{—}M^{(III-\delta)}\text{—}]_n$ chain, and refer to the simple NN mass-and-spring model illustrated in the upper part of Fig. 2. Lattice dynamics then predicts one acoustic and three optical intrachain longitudinal phonon branches for this four-atom unit cell ($\beta=A$, R, $IR1$, and $IR2$). At the zone center ($q=0$) one of the optic modes is Raman (R) active and the other two are infrared (IR) active.[3] The normal coordinates (Q_β) and momenta (P_β) for these zone-center modes can be written as

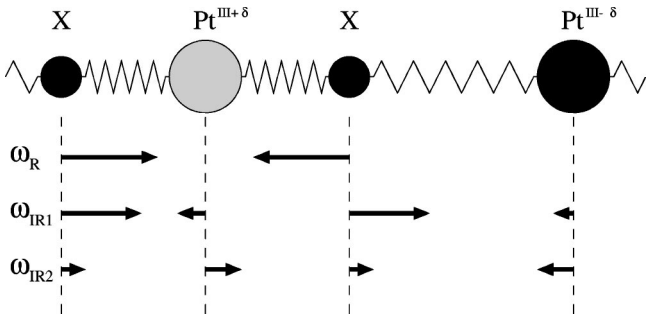

FIG. 2. Lattice displacements for the three zero-wave-vector longitudinal Raman and infrared optical phonon modes in a Pt_2X_2 unit cell.

$$Q_\beta=N^{-1/2}\sum_\alpha M_\alpha^{1/2}\{\mathbf{e}_\beta\}_\alpha\{\mathbf{x}\}_\alpha,\quad P_\beta=\dot{Q}_\beta, \tag{2}$$

where $\{\mathbf{x}\}_\alpha$ and M_α are the actual ion displacements and ion masses, respectively. For the case of a PtCl chain, the corresponding frequencies and eigenvectors are listed in Table I.

Introducing, as usual, phonon creation and destruction operators

$$b_\beta^{(\dagger)}=\left(\frac{\omega_\beta}{2\hbar}\right)^{1/2}Q_\beta+i^{(*)}\left(\frac{1}{2\hbar\omega_\beta}\right)^{1/2}P_\beta, \tag{3}$$

the coupling of the MX electron system to the Raman- and IR-phonon modes takes the form

$$\begin{aligned}\mathcal{H}_{\text{el-ph}}=&\lambda_R(b_R+b_R^\dagger)\sum_l(n_{l2}-n_{l4})\\&+\lambda_{\rm IR1}(b_{\rm IR1}+b_{\rm IR1}^\dagger)\sum_l(n_{l2}+n_{l4}-n_{l1}-n_{l3})\\&+\lambda_{\rm IR2}(b_{\rm IR2}+b_{\rm IR2}^\dagger)\sum_l(n_{l3}-n_{l1}+n_{l2}+n_{l4})\end{aligned} \tag{4}$$

TABLE I. Frequencies and eigenvectors of the zone-center ($q=0$) acoustic and optical (R and IR active) phonon modes of a PtCl MX chain. Results are obtained by fitting the force constants to the Raman and IR spectra of a PtCl chain (Ref. 4). The corresponding lattice displacements of the optical modes are sketched in Fig. 1.

β	$\omega_\beta[s^{-1}]$	$\overline{\nu}_\beta[cm^{-1}]$	$\{\mathbf{e}_\beta\}_\alpha$
A	0	0	(0.276, 0.651, 0.276, 0.651)
R	$5.879\cdot10^{13}$	312	(0.707, 0, −0.707, 0)
IR1	$6.728\cdot10^{13}$	357	(0.627, −0.455, 0.627, −0.077)
IR2	$2.882\cdot10^{13}$	153	(0.174, 0.608, 0.174, −0.755)

(λ_β denote the interaction constants), and

$$\mathcal{H}_{\rm ph}=\hbar\omega_R b_R^\dagger b_R+\hbar\omega_{\rm IR1} b_{\rm IR1}^\dagger b_{\rm IR1}+\hbar\omega_{\rm IR2} b_{\rm IR2}^\dagger b_{\rm IR2}, \quad (5)$$

is the lattice contribution in harmonic approximation. Then

$$\mathcal{H}^{\rm PHM}=\mathcal{H}_{\rm el}+\mathcal{H}_{\rm el\text{-}ph}+\mathcal{H}_{\rm ph} \quad (6)$$

constitutes the so-called *Peierls-Hubbard model* (PHM).

The sets of parameters capable of describing Pt and Ni-based MX materials in the framework of the Su *et al.*[13] model and related one- and two-band models have been estimated from comparison to band structure calculations[2,5,14,15] [more recent local-density-approximation (LDA) results including the ammonia ligands can be found in Ref. 16]. Within the PHM, for the PtCl CDW system, $\Delta=1.2$, $U_{\rm Pt}=0.8$, $U_{\rm Cl}=0$, $\hbar\omega_R=0.05$, $\hbar\omega_{\rm IR1}=0.06$, and $\hbar\omega_{\rm IR2}=0.024$ seem to be appropriate,[17] where the energy scale is given by the NN transfer element $t=1.54$ eV (cf. also Refs. 2 and 4).

Besides modeling real MX chain materials, the PHM is a generic many-body model that is interesting in its own right, mainly because it accounts for several competing effects which are of general importance in low-dimensional solids. First of all the PHM interpolates between the small-Δ limit, where the M-X hybridization cannot be neglected, and a pronounced charge-transfer (CT) situation at large Δ. In particular, for the latter case, where an effective one-band description might be possible, the itineracy of the electrons ($\propto t$) strongly competes with the electron-electron (U) and electron-phonon (λ_R) interactions, which tend to localize the charge carriers by establishing SDW and CDW correlations on the metal sites, respectively. As a result, at half-filling, even a metal-insulator transition of the Mott or Peierls type can take place, depending on the relative strength of the Hubbard and electron-phonon interactions. The spontaneous Peierls dimerization transition to a less symmetric, but lower-energy, configuration definitely takes place at temperature $T=0$ in the *adiabatic* limit (at least for $U=0$). It is well known, however, that in a wide range of quasi-one-dimensional metals, the lattice zero-point motion is comparable to the Peierls lattice distortion, which makes the rigid lattice approximation questionable.[18–20] The PHM is clearly a prototype model with which to study the problem concerning the stability of the Peierls-distorted ground state against quantum phonon fluctuations. Moreover, any theoretical analysis of the unconventional transport and optical phenomena observed in low-dimensional CDW systems has to be based on such a type of dynamically coupled electron-phonon model.

Motivated by this situation, in the following sections, we carry out a comprehensive exact diagonalization study of the PHM, treating the electron and phonon degrees of freedom on an equal footing. To this end, we consider the PHM on an eight-site lattice with periodic boundary conditions,[21,22] and focus on the physically most interesting 3/4-filled band case. If not otherwise stated, we use the PtCl parameter set quoted above.

III. GROUND STATES

To understand the consequences of a dynamical electron-phonon interaction for our two-band model, we first examine the ground-state properties of the PHM. Besides the various contributions to the ground-state energy (E_0), $E_{\rm ph}=\langle\mathcal{H}_{\rm ph}\rangle$, $E_{\rm el\text{-}ph}=\langle\mathcal{H}_{\rm el\text{-}ph}\rangle$, and $E_{\rm el}=\langle\mathcal{H}_{\rm el}\rangle$, with

$$E_{\rm kin}=-t\sum_{\langle l\alpha,l'\alpha'\rangle\sigma}\langle c_{l\alpha\sigma}^\dagger c_{l'\alpha'\sigma}\rangle, \quad (7)$$

$$E_\Delta=\sum_{l\alpha\sigma}\varepsilon_\alpha\langle n_{l\alpha\sigma}\rangle, \quad (8)$$

$$E_U=\sum_{l\alpha}U_\alpha\langle n_{l\alpha\uparrow}n_{l\alpha\downarrow}\rangle, \quad (9)$$

physical quantities of interest are the local particle occupation numbers

$$n_i=\langle(n_{i\uparrow}+n_{i\downarrow})\rangle, \quad (10)$$

the local magnetic moments[23]

$$L_i=\frac{3}{4}\langle(n_{i\uparrow}-n_{i\downarrow})^2\rangle, \quad (11)$$

the NN bond order parameters

$$p_{i-(i+1)}^{\rm Pt=Cl}=\frac{1}{2}\sum_\sigma\langle c_{i\sigma}^\dagger c_{i+1\,\sigma}+c_{i+1\,\sigma}^\dagger c_{i\sigma}\rangle, \quad (12)$$

with $\Sigma_{i=1}^N p_{i-(i+1)}^{\rm Pt=Cl}=-E_{\rm kin}/2t$, and the spin and charge structure factors

$$S_s(q)=\frac{1}{N}\sum_{i,j}\langle S_i^z S_j^z\rangle e^{iq(i-j)} \quad (13)$$

and

$$S_c(q)=\frac{1}{N}\sum_{i,j}[\langle n_i n_j\rangle-n_i^2]e^{iq(i-j)}, \quad (14)$$

respectively. Here, $i,j=1,\ldots,N$ renumber the lattice sites and $\langle\cdots\rangle=\langle\psi_0|\cdots|\psi_0\rangle$. Additional useful information can be obtained from the so-called phonon distribution function[24] [for notation, see Appendix A, Eq. (A1)]

$$C_\beta^{(M)}(m)=\sum_{\substack{r,s\\ \{m_\beta^s=m\}}}|c_{r,s}^\psi|^2, \quad (15)$$

which gives the relative weight of the m-phonon state of the β-phonon mode in state $|\psi\rangle$. The normalization of $|\psi\rangle$ implies $\Sigma_{m=0}^M C_\beta^{(M)}(m)=1$.

Table II presents our exact diagonalization results obtained for the $N=8$ site PHM at selected electron-phonon couplings (in what follows SMA and DMA denote single-[$\lambda_{\rm IR1}=\lambda_{\rm IR2}=0$] and double-mode [$\lambda_{\rm IR2}=0$] approximations, respectively). In the noninteracting case ($\lambda_\beta\equiv 0$; first column), the partial densities and charge structure factor $S_c(\pi)$ reflect the CT ($\Delta=1.2$) from metal (M) to halide (X)

TABLE II. Energy contributions to the ground-state energy (E_0), lattice displacement ($\langle Q_R \rangle$), particle densities (n_i), local magnetic moments (L_i), and bond-order parameters (p_{i-j}), as well as spin (S_s) and charge (S_c) structure factors at $q=\pi/2,\ \pi$ in the ground state of the 3/4-filled Peierls-Hubbard (MX) chain model ($N=8$).

λ_R	0.0	0.05	0.1	0.1
λ_{IR1}	0.0	0.0	0.0	0.026
E_0	−6.0889	−6.0910	−6.6928	−6.7636
E_{el}	−6.0889	−6.0867	−4.9454	−4.8749
E_{ph}	0.0000	0.0002	1.7386	1.8795
$E_{\mathrm{el\text{-}ph}}$	0.0000	−0.0045	−3.4860	−3.7682
E_{kin}	−5.9152	−5.9133	−5.0294	-4.9083
E_Δ	−1.1738	−1.1741	−1.4750	−1.5245
E_U	1.0000	1.0007	1.5590	1.5578
$\langle Q_R \rangle$	0.0000	0.0000	11.7916	12.0206
$n^X_{1,3}$	1.7445	1.7446	1.8073	1.8176
n^M_2	1.2555	1.2554	0.4557	0.4311
n^M_4	1.2555	1.2554	1.9297	1.9337
$L^X_{1,3}$	0.1627	0.1627	0.1323	0.1259
L^M_2	0.4728	0.4725	0.2760	0.2645
L^M_4	0.4728	0.4725	0.0515	0.0487
$p^{M\leftrightharpoons X}_{(1-2,2-3)}$	0.3697	0.3696	0.5410	0.5307
$p^{M\leftrightharpoons X}_{(3-4,4-5)}$	0.3697	0.3696	0.0877	0.0829
$S_s(\pi/2)$	0.1905	0.1903	0.0573	0.0547
$S_s(\pi)$	0.0950	0.0951	0.0797	0.0763
$S_c(\pi/2)$	0.3250	0.3258	1.3045	1.3375
$S_c(\pi)$	0.8533	0.8534	1.0562	1.0959
config.:	●-↑-●-↓	●-↑-●-↓	●-○-●-↑↓	●-○-●-↑↓

sites. The Hubbard interaction ($U=0.8$), acting on metal sites only, gives rise to both large local magnetic moments and a maximum in the magnetic structure factor $S_s(q)$ at $q=\pi/2$. The resulting SDW ground-state configuration survives the inclusion of a weak electron-phonon interaction (second column of Table II), a situation which is realized in the Ni-based materials. If the coupling to the R-active mode becomes stronger, a CDW is formed on the metal sites [cf. the large increase of $S_c(\pi/2)$], accompanied by a decrease of the mobility of the charge carriers (kinetic energy). Now the translational symmetry is spontaneously broken, $\langle Q_R \rangle$ is finite, and the ions vibrate about a new equilibrium position. This is the scenario realized in the PtCl chain system. The CDW is accompanied by a suppression of the local magnetic moments as well as by the formation of a so-called bond-order wave between X^--$M^{\mathrm{III}-\delta}$ and X^--$M^{\mathrm{III}+\delta}$ bonds. Of course, an extreme large electron-phonon coupling will tend to localize the charge carriers completely, and therefore weaken the bond order being maintained by electron hopping processes.

Including a weak coupling to the IR1 mode strengthens the Pt→Cl CT (Ref. 25) and, as a side effect, also the CDW

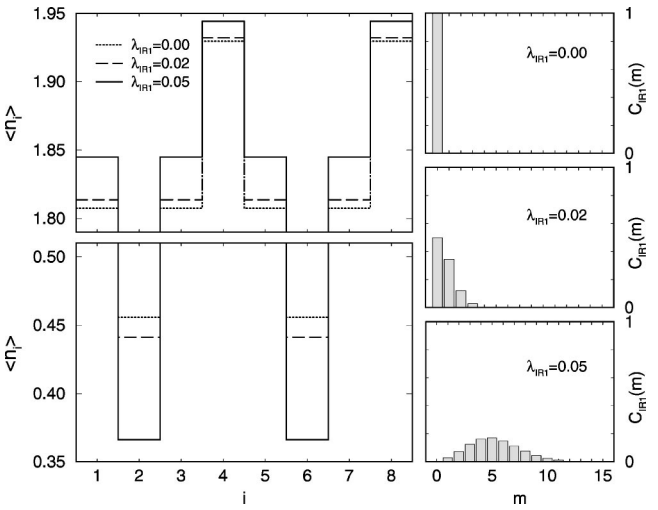

FIG. 3. Shift of the local particle densities with increasing λ_{IR1} (DMA $N=8$:$\lambda_R=0.1$, $\lambda_{\mathrm{IR2}}=0$). The right panels show the corresponding phonon distributions for the IR1 mode in the ground state.

(see fourth column). The influence of both IR-active modes [triple-mode approximation (TMA)] on the local particle densities is illustrated in more detail in Figs. 3 and 4. Obviously, the IR2 mode leads to a disproportionation of the charge density on X sites in the unit cell. The right panels give the phonon distributions of the IR1 (Fig. 3; DMA) and IR2 (Fig. 4; TMA) modes in the ground state. As the electron-phonon coupling strength increases, a shift of the maximum in the phonon distribution to larger values of m is observed, indicating that the ground state becomes a multiphonon state.

IV. EXCITATIONS

A. Low-energy spectrum

In a next step we investigate the low-lying excitations of the PHM model. Figure 5 shows the energy-level diagram within SMA, where the left column displays the spectrum of

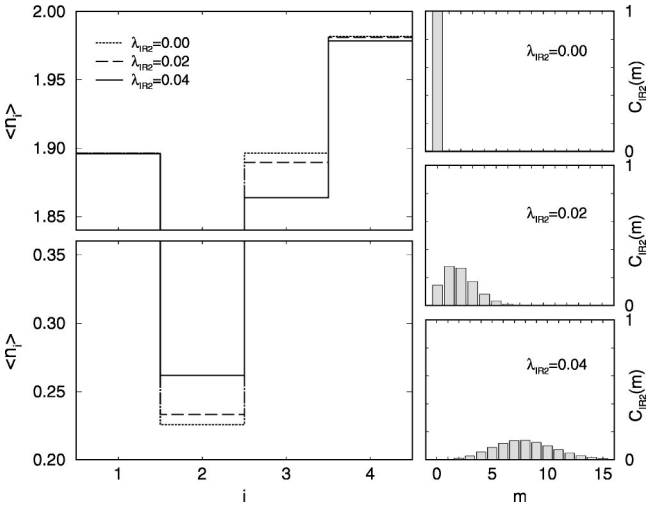

FIG. 4. Shift of the local particle densities as λ_{IR2} increases (TMA $N=4$:$\lambda_R=0.19$, $\lambda_{\mathrm{IR1}}=0.05$). The right panels show the phonon distributions of the IR2 mode in the ground state.

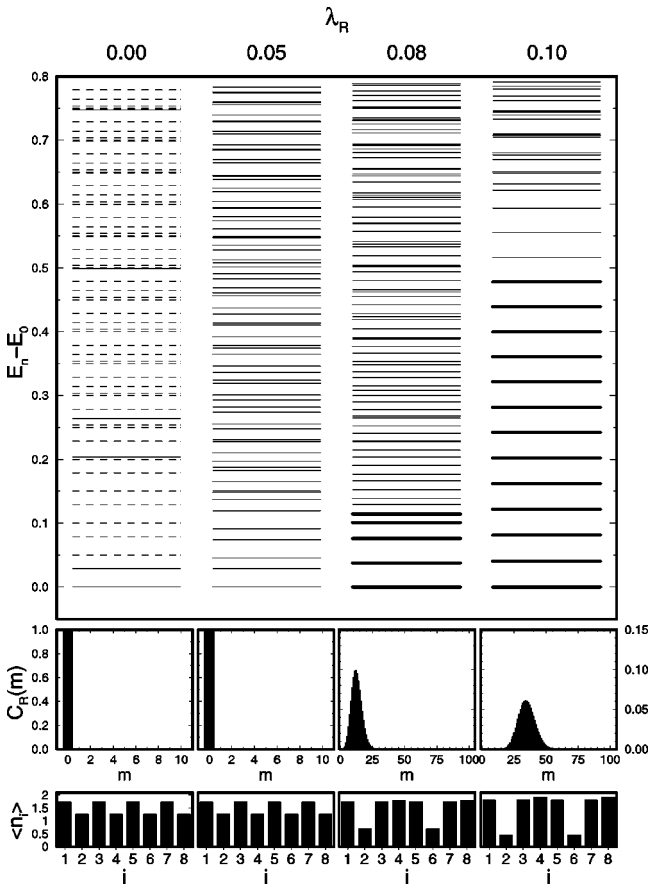

FIG. 5. Low-energy part of the eigenvalue spectrum of the Peierls-Hubbard model (SMA). Twofold degenerate states are marked by bold bars; dashed bars denote the bare phonon overtones of the electronic levels for the $\lambda_R=0$ case. The lower panels give the phonon distribution function and local particle densities in the ground state.

the decoupled system for comparison. Above each electronic level (solid bars) there is a ladder of overtones (dashed bars) with rungs separated by the bare phonon frequency $\hbar\omega_R$. Of course, at any finite electron-phonon coupling, the electron and lattice degrees are no longer independent, and as a result the excitation spectrum is changed. At weak coupling, however, to a good approximation the ground state is still a zero-phonon state, and the states

$$|\tilde{\psi}_R^{(m)}\rangle=\frac{1}{\sqrt{m_R!}}(b_R^\dagger)^{m_R}|\psi_0\rangle^{\mathrm{wc}}$$

have a nearly complete overlap with the exact low-lying excited states of the interacting system, indicating that these excitations can be obtained simply by adding phonons to the ground state. With increasing electron-phonon interaction strength, a strong mixing of electrons and phonons takes place, such that both quantum objects completely lose their individual identity. As a result the ground state is basically a multiphonon state [cf. $C_R(m)$; middle panel]. Note that the ground state and, as λ_R increases, a growing number of excited states show a twofold degeneracy (within numerical accuracy). The reason is the existence of two degenerate

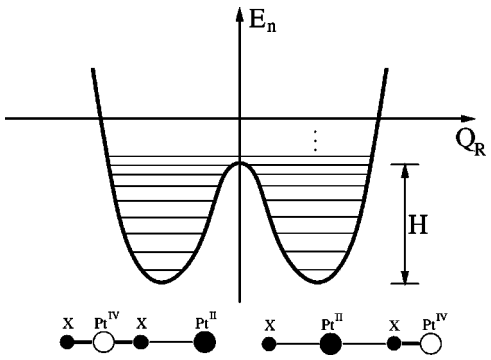

FIG. 6. Sketch of the effective adiabatic double-well potential acting in the strong CDW regime of the Peierls-Hubbard model (for further explanation, see the text).

CDW ground states in the strong-coupling limit, with large spectral weights of the $|\uparrow\downarrow,\uparrow\downarrow,\uparrow\downarrow,0\rangle_{\mathrm{el}}$ or $|\uparrow\downarrow,0,\uparrow\downarrow,\uparrow\downarrow\rangle_{\mathrm{el}}$ electronic basis states. The charge distribution shown in the lower panel of Fig. 5 corresponds to the latter case.

In the configuration space of the Raman-active normal coordinate, this gives rise to the formation of an adiabatic double-well potential (see Fig. 6). Within one minimum of the double-well potential the low-lying excitations exhibit a large overlap with the displaced oscillator states

$$|\tilde{\psi}_R^{(m_R)}\rangle=\frac{1}{\sqrt{m_R!}}(B_R^\dagger)^{m_R}|\psi_0\rangle^{\mathrm{sc}}=|\psi_0\rangle_{\mathrm{el}}^{\mathrm{sc}}\otimes|m_R,\eta_R\rangle_{\mathrm{ph}},$$

where $\eta_R=\lambda_R\Sigma_l\langle n_{l2}-n_{l4}\rangle$ are the constant effective forces in the limit $t\to 0$ and $B_R^{(\dagger)}=b_R^{(\dagger)}-\eta_R/\omega_R$. We have proven this by calculating

$$\Pi_{m_R}(\omega)=\sum_{n=0}^{D_{\mathrm{tot}}-1}|\langle\psi_n|\tilde{\psi}_R^{(m_R)}\rangle|^2\delta(\omega-E_n). \qquad (16)$$

The displaced oscillator spectral function $\Pi_{m_R}(\omega)$ is depicted in Fig. 7. As a consequence of the electron-lattice interaction the multiphonon excitations are somewhat shifted from multiples of the bare phonon frequencies $m_R\times\omega_R$. The lower intensity of the high-energy peaks reflects the incomplete overlap of the higher-order overtone states of the interacting system with the corresponding displaced oscillator wave functions (see the left panel). Going to extremely large electron-phonon couplings, the overlap of these high-energy excitations is clearly improved (cf. the tendency of the results obtained for $\lambda_R=0.9$ and 0.12). The important point we would like to emphasize is the weak *anharmonicity* of the double-well potential even at low energies, provided we consider reasonable coupling strengths. This *nonlinearity*, induced by the coupling to the itinerant *interacting* electron system, is the origin of the redshift of the overtones discussed in the next subsection.

Of course, exciting more and more phonons enhances the tunneling probability between the two minima of the potential, and finally counterbalances the charge difference on Pt sites $\langle n_2-n_4\rangle$ ($\langle Q_R\rangle=0$) by overcoming the potential barrier

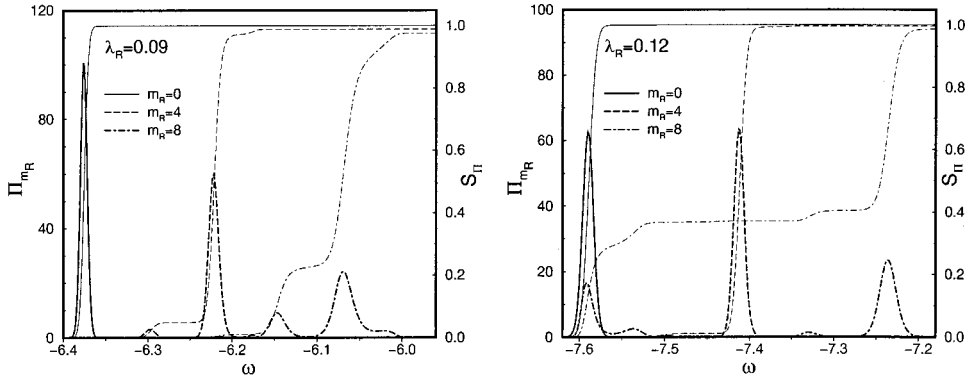

FIG. 7. Phonon spectral function $\Pi_{m_R}(\omega)$ and intergrated weight $S_\Pi(\omega)=\int_{E_0}^{\omega} d\omega' \Pi_{m_R}(\omega')$ in the CDW regime of the PHM.

$$H \simeq m_{R,c}\omega^{(1)}(\lambda_R). \tag{17}$$

Here

$$\omega^{(1)}=E_1-E_0 \tag{18}$$

denotes the fundamental phonon frequency of the strongly interacting system. Figure 8 impressively demonstrates the validity of estimate (17) by showing that $n_c \simeq m_{R,c}$ indeed holds (cf. also Fig. 5; $\lambda_R=0.1$).

The different nature of the excited states in the weak- and strong-coupling cases is reflected in the phonon distribution function displayed in Fig. 9. At weak electron-phonon interactions (left panel), we have a SDW ground state, and the first excited state is an electronic (almost zero-phonon) state above the SDW gap (opened by U). The next states are simply obtained by adding phonons to this doublet, with a slightly reduced frequency compared to ω_R (cf. Fig. 5). In the strongly interacting regime the phonon distribution is clearly evocative of that of a displaced harmonic oscillator.

Although the situation becomes somewhat more complex in the DMA, the basic mechanism are the same. Figure 10 shows the successive excitation of (R,IR1)-active phonons [$n=1$: (1,0), $n=2$: (0,1) $n=3$: (2,0), $n=4$:(1,1)].

B. Intrinsic localized modes

As already pointed out in Sec. I recent resonant Raman scattering measurements on isotopically pure PtCl materials have shown a significant redshift of the overtones.[8] In resonance Raman spectroscopy the material is illuminated with light that is in resonance with a specific electronic transition. The signals from the (fundamental and overtone) vibrational modes that are coupled to the electronic transition are greatly enhanced. Resonant Raman spectra on strong CDW PtCl exhibiting such an amplification were obtained using Ar^+ laser illumination at 514 nm, which roughly corresponds to the bandedge ($\approx$2.5 eV) of an intervalence charge transfer (IVCT) transition between Pt^{II} and Pt^{IV} (see Fig. 11). The photoexcited transition into the IVCT band is connected with the excitation of the fundamental Raman active symmetric Cl-Pt-Cl stretch and a progression of many overtones.

In order to understand the evolution of the experimentally observed overtone structure,[8] let us first discuss the level shift of the nth excited R-active doublet,

$$r_n=\frac{n\omega_R^{(1)}-\omega_R^{(n)}}{\omega_R^{(1)}}, \tag{19}$$

with $\omega_R^{(n)}=(E_n-E_0)$, in the framework of the nonadiabatic PHM. Figure 12 displays the calculated redshifts r_n for different couplings λ_R at $U_{\mathrm{Pt}}=0.8$. Obviously a noticeable *redshift* is observed in a certain coupling regime only. The reason for this is the following: On the one hand, a critical interaction strength λ_R is necessary to overcome the SDW configuration forced by U, and to establish a (degenerate)

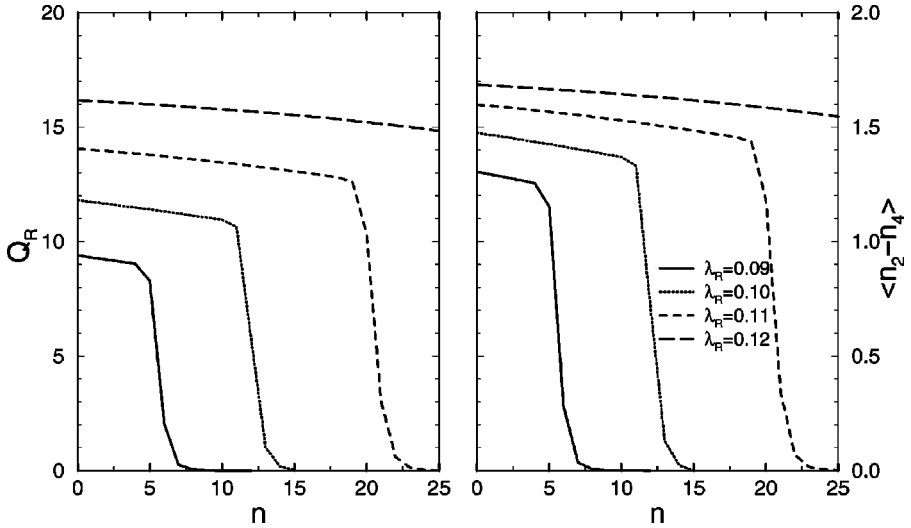

FIG. 8. Expectation values of the Raman-mode lattice displacements (left panel) and differences of the mean electron densities on the two Pt sites (in an unit cell) are given for the lowest 25 eigenstates $|\psi_n\rangle$ within the SMA.

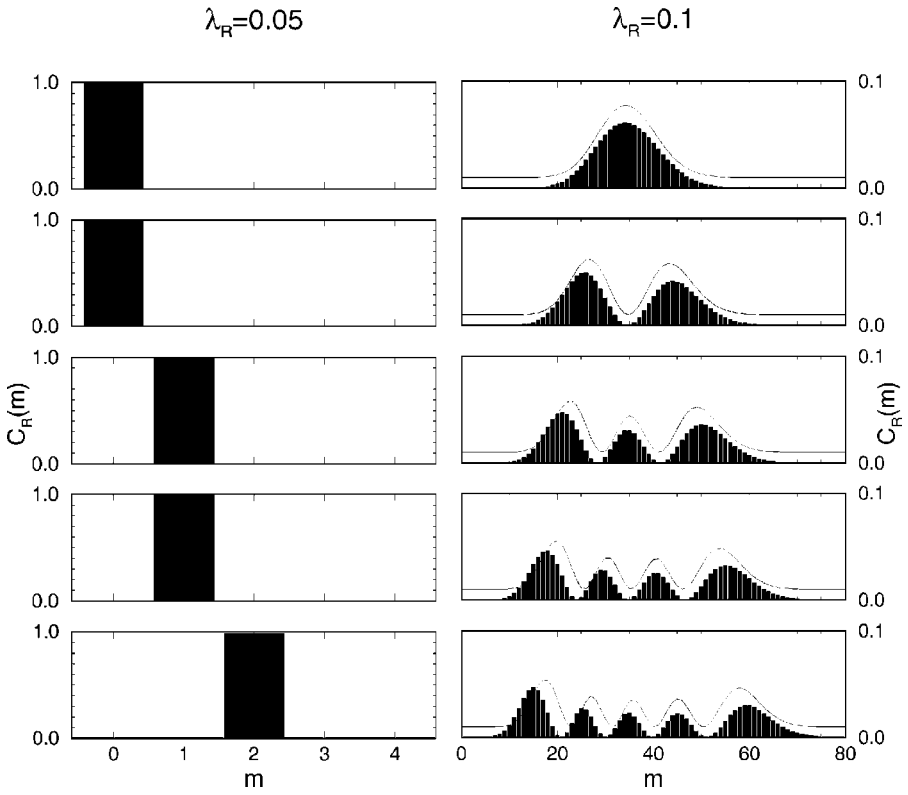

FIG. 9. Phonon distribution in the ground state and in the lowest four excited states of the Peierls-Hubbard model (from top to bottom). The solid lines, displayed for clarity with an offset of the ordinate of 0.01 in the right panels, corresponds to the $t=0$ displaced oscillator limit. Results are obtained within the SMA.

multiphonon CDW ground state (cf. Fig. 5). On the other hand, at extremely large couplings, the particles are completely trapped and with respectly to the lattice excitations the system behaves as an almost perfect displaced *harmonic* oscillator. This is corroborated by the variation of the Raman fundamental $\omega_R^{(1)}$ [cf. Eq. (18)], shown in the inset. In particular, one realizes that $\lim_{\lambda_R\to\infty}\omega_R^{(1)}(\lambda_R)=\omega_R$. In the intermediate (but still strong-coupling) region, the Raman-active mode dynamically self-generates a *nonharmonic*

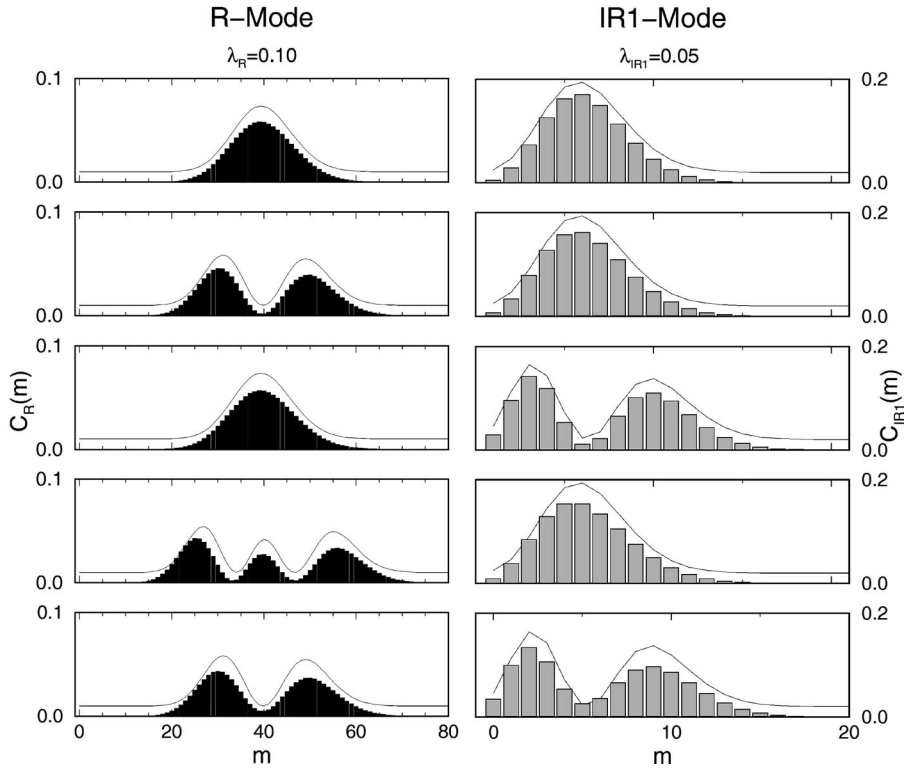

FIG. 10. Phonon distribution in the ground state and in the lowest four excited states, as presented in Fig. 9, but within the DMA.

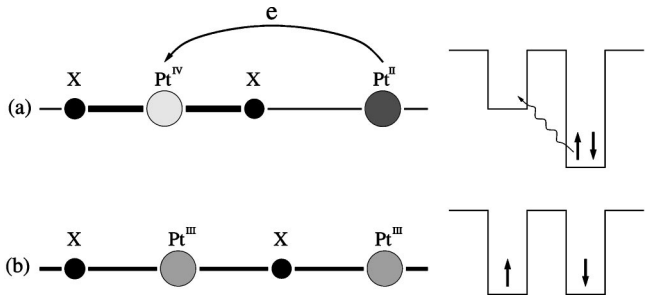

FIG. 11. Mixed-valence ground state and IVCT to an excited state without charge disproportionation (a); lattice relaxation and formation of a charge-transfer exciton (b).

lattice potential, providing an attractive interaction of Raman phonon quanta located at the same Pt_2Cl_2 unit, with the result that quasilocalized multiphonon bound states occur in the system. Translational symmetry is restored by a quantum-mechanical tunneling of those quasiparticles. A nearly perfect quantitative reproduction of the redshift observed in PtCl was obtained by applying the DMA with $\lambda_R = 0.1$ and $\lambda_{IR1} = 0.026$ (see Fig. 12).

It is interesting to contrast these findings with the results obtained for $U=0$ (see Fig. 13). Here a CDW with lattice dimerization is already formed in the weak-coupling regime, i.e., states with wave numbers 0 and π are degenerate even for small values of λ_R (at least in the thermodynamic limit $N\rightarrow\infty$). Therefore, the ground state as well as the excitations contain only a few phonons, and may be viewed as ''conventional'' Peierls states. In fact, at $\lambda_R = 0.06$, all phonon distributions corresponding to excited states with $n \leqslant 2$ exhibit pronounced maxima at $m=0$. Remarkably we found a *blueshift* ($r_n < 0$) of the overtones in this regime. Increasing the electron-phonon interaction, the charge carriers become heavily dressed by phonons, and finally a self-trapping transition takes place. As a result localized multiphonon bound states occur and r_n becomes positive. At this point it seems reasonable to make contact with polaron physics and consider the CDW state at large λ_R as built up by ordered bipolarons residing at the $Pt^{III-\delta}$ sites.

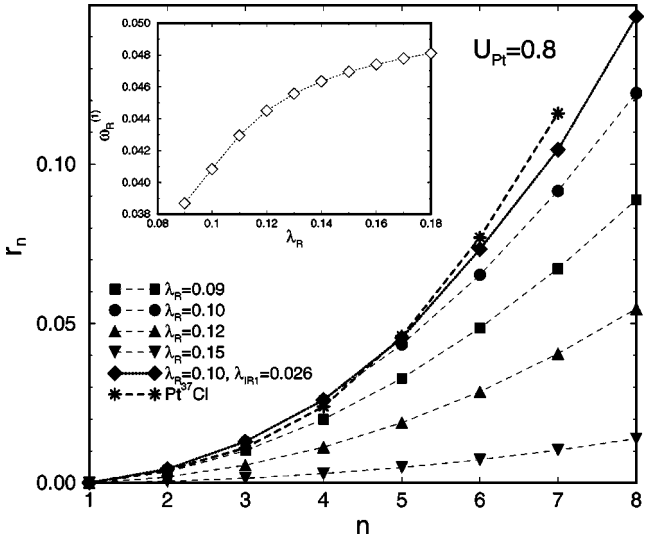

FIG. 12. Relative redshift of the lowest-energy peaks, normalized by the fundamental frequency $\omega_R^{(1)}$ given in the inset, as a function of the final quanta of the vibrational energy. Results are obtained for an eight-site chain with different coupling strengths λ_R at $\lambda_{IR1,IR2}=0$ if not otherwise stated.

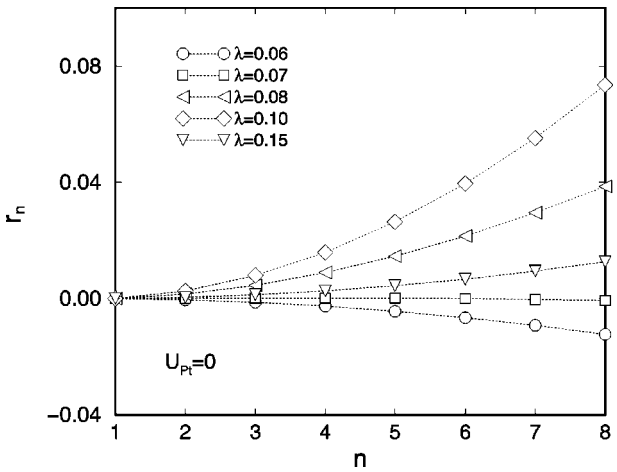

FIG. 13. Shift of the lowest-energy peaks, as presented in Fig. 12, but for $U_{Pt}=0 (\lambda \equiv \lambda_R)$. Note the blueshift at lower electron-phonon couplings.

C. Optical response

To substantiate the interpretation that the strong-coupling CDW ground state of the 3/4 filled PHM describes ordered bipolarons rather than a Peierls band insulator, in this section we study the optical conductivity. In linear response theory the regular part of the optical conductivity,

$$\sigma_{\mathrm{p}}^{\mathrm{reg}}(\omega) = \frac{\pi}{N} \sum_{m\neq 0} \frac{|\langle \psi_0 | \hat{j}_{\mathrm{p}} | \psi_m \rangle|^2}{E_m - E_0} \delta[\omega - (E_m - E_0)], \tag{20}$$

gives the incoherent contribution of the optical transport. Equation (20) is equivalent to the small polaron hopping conductivity in the strong electron-phonon coupling limit. According to the *f*-sum rule,

$$2\int_0^\infty d\omega' \sigma_{\mathrm{p}}^{\mathrm{reg}}(\omega') = -\sigma_0 E_{\mathrm{kin}} - \mathcal{D}, \tag{21}$$

it is related to the kinetic energy E_{kin} [cf. Eq. (7)] and the Drude weight $\mathcal{D}$ ($\sigma_0 = \pi e^2$; periodic boundary conditions). In Eq. (20), the (paramagnetic) current density operator is

$$\hat{j}_{\mathrm{p}} = -iet \sum_{i\sigma} (c_{i\sigma}^\dagger c_{i+1\,\sigma} - c_{i+1\,\sigma}^\dagger c_{i\sigma}). \tag{22}$$

In analogy one can define a current operator for NN hopping processes of on-site electron pairs (bipolarons) as

$$j_{\mathrm{bp}} = -i2et \sum_i (C_i^\dagger C_{i+1} - C_{i+1}^\dagger C_i), \tag{23}$$

with $C_i^{(\dagger)} = c_{\uparrow i}^{(\dagger)} c_{\downarrow i}^{(\dagger)}$, which gives rise to a bipolaronic optical conductivity $\sigma_{\mathrm{bp}}^{\mathrm{reg}}(\omega)$. In addition, we consider higher-

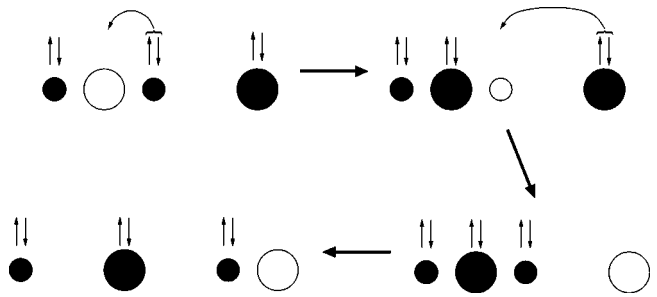

FIG. 14. Regular part of the optical conductivity $\sigma^{\mathrm{reg}}(\omega)$ (solid lines), normalized by σ_0/N, and integrated spectral weight S^{reg} (dot-dashed lines) are shown for weak to strong electron-phonon couplings (SMA, PBC).

order next-nearest-neighbor (NNN) bipolaron transport processes (see Fig. 14), relating the two degenerate ground-state configurations of an unit cell (cf. Fig. 6). The corresponding transfer operator is

$$C_3^\dagger C_4 C_2^\dagger C_3 := c_{3\uparrow}^\dagger c_{3\downarrow}^\dagger c_{4\downarrow} c_{4\uparrow} c_{2\uparrow}^\dagger c_{2\downarrow}^\dagger c_{3\downarrow} c_{3\uparrow}, \tag{24}$$

leading to $\sigma_{\mathrm{bp,NNN}}^{\mathrm{reg}}(\omega)$, with

$$j_{\mathrm{bp,NNN}} \propto \sum_{i\ \mathrm{even}} (C_{i+1}^\dagger C_{i+2} C_i^\dagger C_{i+1} - C_{i+1}^\dagger C_i C_{i+2}^\dagger C_{i+1}). \tag{25}$$

At first, however, let us consider the behavior of the more usual optical conductivity $\sigma_{\mathrm{p}}^{\mathrm{reg}}(\omega)$. Figure 15 gives $\sigma_{\mathrm{p}}^{\mathrm{reg}}(\omega)$ at several characteristic coupling strengths. In the absence of any scattering mechanisms the optical conductivity simply consists of the Drude peak at $\omega=0$; i.e., for noninteracting band electrons, there is no optical absorption at finite frequencies. In contrast, the interacting two-band Hubbard model [Eq. (1)] contains finite-frequency optical transitions (see Fig. 15, left panel: $\lambda_R=0$ case). Specifically, the principal optical excitations of model (1) are transitions across the SDW (lower peak at about $\omega=0.28$) and the M-X CT gap (upper peak about $\omega=3.5$). The integrated spectral weight $S^{\mathrm{reg}}(\omega)=\int_\infty^\omega d\omega' \sigma^{\mathrm{reg}}(\omega')$ indicates that the optically induced M-X interband transition has a negligible intensity compared with the low-energy excitation between the M-M SDW bands split up by U. Including a weak electron-phonon coupling has two main effects (see the results for $\lambda_R=0.7$). First, the low-energy peak is broadened because now phonon degrees of freedoms are involved in the excitations. Secondly λ_R tends to open a CDW gap and therefore weakens the SDW gap (i.e., Peierls versus Mott-Hubbard scenario). At $\lambda_R=0.9$ the CDW is energetically more favorable than a SDW ground state. Now the first excitation is due to an IVCT M-M transition. The optical CDW gap enlarges as λ_R further increases. At the same time the optical response develops clear signatures of polaronic excitations. Clearly the line shape of the first peak in $\sigma_p^{\mathrm{reg}}(\omega)$ reflects the phonon distribution of the ground state.

Experimentally, for the PtI-PtBr-PtCl sequence of PtX materials one observes a decrease in height and shift to higher energies of the IVCT absorption peak.[2,26] Since the

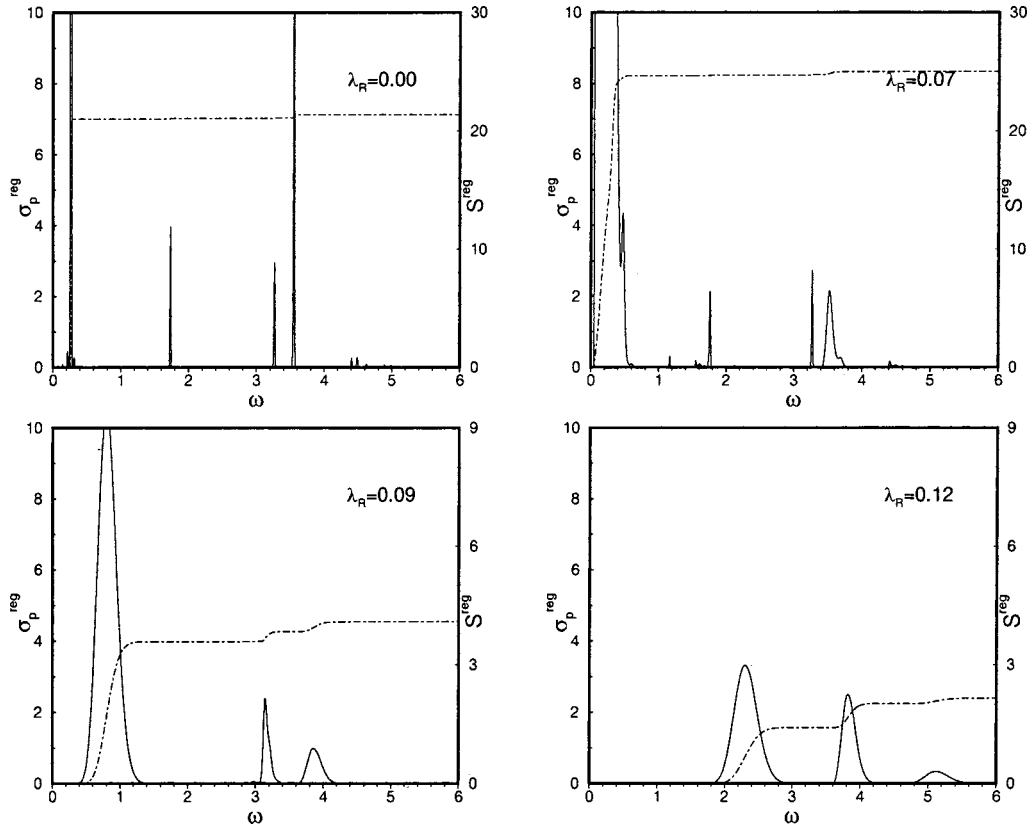

FIG. 15. Hopping conductivity of bipolarons in the Peierls-Hubbard model.

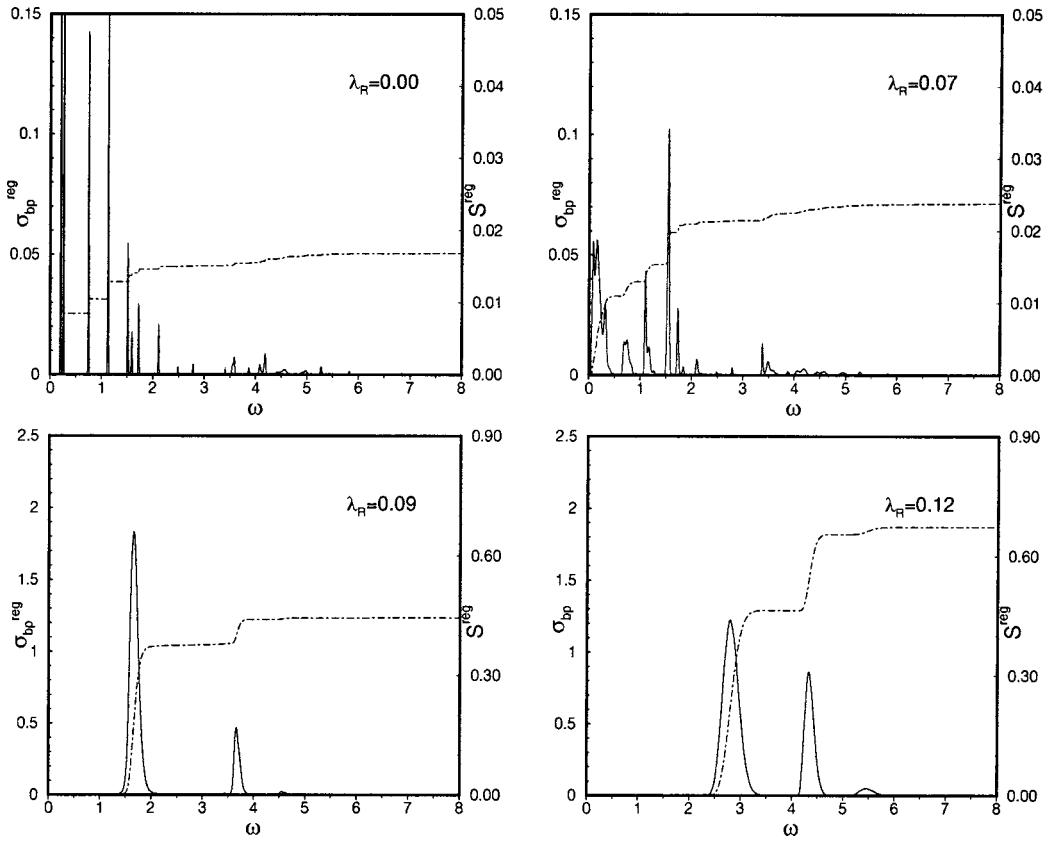

FIG. 16. Second-order bipolaron transfer between Pt sites.

major difference between the members of this class seems to be the different strength of the electron-lattice coupling, which increases in going from the I halide to the Cl halide, our results provide a microscopic explanation of this observation. Using $\lambda_R = 0.09 \ldots 0.1$ for the PtCl chain compound, the calculated position of the low-energy peak at about 2.6 eV ($t = 1.54$ eV was taken into account) is found even in quantitative agreement with experiments. Moreover, there is evidence for the CT *M*-*X* transition near 5.5 eV in the reflectivity data for PtCl,[26] where the *M*-*X* transition is expected to be quite strong in the strongly distorted PtCl system, while in the weakly distorted PtI material it is very weak.[2] Naturally these findings were qualitatively reproduced by our model calculation as well.

The optical-absorption spectrum for bipolarons is shown in Fig. 16. As expected, the spectral weight of bipolaronic excitations is extremely small at weak electron-phonon interactions. According to the results of Secs. IV A and IV B, a bipolaronic CDW insulator is formed in the strong-coupling limit. Since the bipolaron current operator connects only states having a substantial overlap as far as the phononic contribution is concerned, in this limit multiphonon absorptions become increasingly important in the optical response, leading to the peak structure depicted in the lower panels. Compared with the single-polaron conductivity $\sigma_{\mathrm{p}}^{\mathrm{reg}}(\omega)$ the low-energy peak is shifted to larger frequencies. This can be easily understood within polaron transport theory. During a NN transfer process the polaronic charge carrier has to overcome the self-induced potential barrier at the initial site, and after the hop a local lattice distortion has to be created on the neighboring site. In the nonadiabatic regime this leads to an absorption maximum in $\sigma_{\mathrm{bp}}^{\mathrm{reg}}(\omega)$ at $2E_{\mathrm{bp}} \simeq 2 \times 2E_{\mathrm{p}}$, where E_{bp} (E_{p}) is the bipolaron (polaron) binding energy. In fact a similar mechanism acts in the adiabatic case as well. Here the low-lying peak position's roughly equals to four times the barrier height H of the effective adiabatic double-well potential (see Figs. 6 and 5, which gives the estimate $H \simeq 0.45$ for $\lambda_R = 0.1$).

Of special interest are those transport processes which directly connect the two degenerate ground states of the CDW (cf. Figs. 6 and 14). Results for the optical conductivity $\sigma_{\mathrm{bp,NNN}}^{\mathrm{reg}}(\omega)$, describing such types of excitations, are presented in Fig. 17. Applying the eight electron creation and annihilation operators [Eq. (24)] on the ground state strongly filters the intermediate excited states contributing to $\sigma_{\mathrm{bp,NNN}}^{\mathrm{reg}}(\omega)$. This means that only those activated states having a large overlap with the $\mathrm{Pt^{II}}$-$\mathrm{Pt^{IV}}$ basis states $|\uparrow\downarrow,\uparrow\downarrow,\uparrow\downarrow,0\rangle_{\mathrm{el}}$ and $|\uparrow\downarrow,0,\uparrow\downarrow,\uparrow\downarrow\rangle_{\mathrm{el}}$ acquire a large spectral weight. This is perfectly demonstrated by the lower right panel of Fig. 17. A comparison of the intermediate ($\lambda_R = 0.09$) and strong-coupling ($\lambda_R = 0.12$) results obtained for $\sigma_p^{\mathrm{reg}}(\omega)$ (Fig. 15), $\sigma_{bp}^{\mathrm{reg}}(\omega)$ (Fig. 16), and $\sigma_{\mathrm{bp,NNN}}^{\mathrm{reg}}(\omega)$ (Fig. 17) reaffirms the interpretation of the strong-coupling CDW state in PtCl in terms of a charge-ordered bipolaronic insulator.

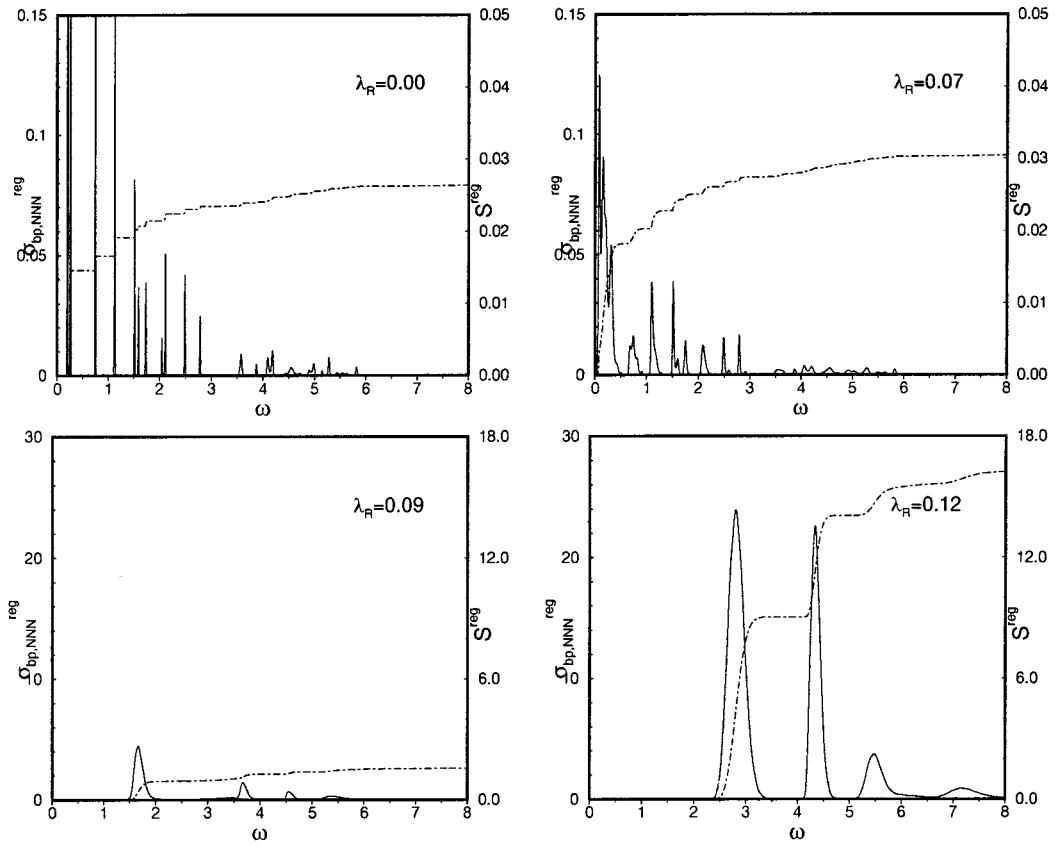

FIG. 17. Higher-order contributions to the bipolaronic optical response. Results are presented for the same parameters as in Fig. 15, but note the different scale of the ordinate in the strong-coupling regime.

V. CONCLUSIONS

To summarize, in this paper we have presented a comprehensive study of the 3/4-filled, two-band, one-dimensional Peierls-Hubbard model, which we believe captures the essential physics of the *MX* family of halogen-bridged transition-metal compounds. We mainly analyzed phenomena resulting from the complex interplay of charge, spin, and lattice degrees of freedom existing in these low-dimensional highly correlated materials. The formation of Peierls distorted phases with predominantly charge- or spin-density-wave order or the intrinsic localization of vibrational energy in multiphonon bound states are such phenomena. In doing so, the basic necessity for correctly taking into account both the electronic correlations as well as the dynamics and quantum nature of the phonons leads us to a purely numerical approach. We applied a high-resolution Jacobi-Davidson algorithm, and solved the fully nonadiabatic Peierls-Hubbard model exactly on finite lattices. Focusing on situations where the dominant effects of the electron-electron and electron-phonon interactions are short ranged, such a finite-cluster calculation seems to be justifiable.

From this perspective our approach is particularly suitable for the strong CDW material PtCl, because in this compound the CDW coherence length is of the order of the lattice constant, i.e., local lattice effects predominate. In fact we showed that PtCl typifies a charge-ordered bipolaronic insulator rather than a traditional Peierls band insulator. The necessity of a substantial coupling to the Raman active phonon mode to overcome the notable on-site Coulomb repulsion on the Pt sites in the CDW state is a clear indication of this. As a consequence of the strong electron-phonon interaction, the charge carriers are heavily dressed by phonons, and finally trapped in pairs as bipolarons on the lattice. The residual weak itinerancy of the bipolarons maintains the translational symmetry and produces an effective interunit coupling, which is the condition preceding the formation of a CDW. We emphasize that the adiabatic bipolarons discussed in this context differ in nature to a certain extent from the small electronic bipolarons normally formed in the antiadiabatic strong-coupling low-carrier-density limit. In view of the underlying physical mechanism, perhaps they should rather be interpreted as *vibrational (bi)polarons* being localized in a single PtCl unit. At appropriate electron-phonon interaction strengths, the effective lattice potential, dynamically self-generated in the process of carrier localization, exhibits a significant nonlinearity, leading to the experimentally observed localization of vibrational energy in PtCl. As a characteristic feature the overtones of these *intrinsic localized modes* show a strong redshift, which we were able to reproduce even quantitatively by our finite-lattice calculation. The localized nature of these vibrational excitations, which are coupled to the intervalence charge transfer transition between Pt^{II} and Pt^{IV}, was further supported by the results obtained for the phonon spectral function and the optical (bipolaronic) response.

In conclusion, we have shown that a dynamical coupling to the Raman- and infrared-active phonon modes, even in the adiabatic strong-coupling regime, strongly influences the ground-state and spectral properties of the Peierls-Hubbard model. From a theoretical point of view, the intermediate coupling and frequency regime, where phononic and electronic energy scales are not well separated, is of course even more interesting but less understood. In principle our exact diagonalization approach allows us to tackle this much more complex problem as well. Work in this direction will be reported in the future.

ACKNOWLEDGMENTS

The authors would like to thank A. Basermann, H. Büttner, E. Jeckelmann, A. P. Kampf, J. Loos, A. Saxena, B. Swanson, M. I. Salkola, and A. Weiße for valuable discussions. The research was granted by the DFG-Schwerpunkt 1073. The numerical calculations were performed at LRZ München, NIC Jülich, and HLR Stuttgart. H. F. and G. W. acknowledge the hospitality at the Theoretical Division of Los Alamos National Laboratory. Work at Los Alamos was performed under the auspices of the U.S. DOE.

APPENDIX A: ELECTRON-PHONON BASIS

A general state of the Peierls-Hubbard model [Eq. (6)],

$$|\psi\rangle=\sum_{r=1}^{D_{\mathrm{el}}}\sum_{s=1}^{D_{\mathrm{ph}}} c_{r,s}^{\psi}\{|r\rangle_{\mathrm{el}}\otimes|s\rangle_{\mathrm{ph}}\}, \tag{A1}$$

constitutes a tensor product of electron and phonon states

$$|r\rangle_{\mathrm{el}}=\prod_{i=1}^{N}(c_{i\uparrow}^{\dagger})^{n_{i\uparrow}^{r}}(c_{i\downarrow}^{\dagger})^{n_{i\downarrow}^{r}}|0\rangle_{\mathrm{el}}, \tag{A2}$$

$$|s\rangle_{\mathrm{ph}}=\prod_{\beta=1}^{G}\frac{1}{\sqrt{m_{\beta}^{s}!}}(b_{\beta}^{\dagger})^{m_{\beta}^{s}}|0\rangle_{\mathrm{ph}}, \tag{A3}$$

where $r=1,\ldots,D_{\mathrm{el}}$ and $s=1,\ldots,D_{\mathrm{ph}}$ label the unsymmetrized basis states of the electronic and phononic subspaces with dimensions

$$D_{\mathrm{el}}=\binom{N}{N_{\uparrow}}\binom{N}{N_{\downarrow}}$$

and

$$D_{\mathrm{ph}}^{(M)}=\binom{M+G}{M}$$

($G=1,2,3$ for SMA, DMA, and TMA), respectively. The usual fermion and boson commutation rules imply the occupation numbers $n_{i\downarrow}^{r},n_{i\downarrow}^{r}\in\{0,1\}$ and $m_{\beta}^{s}\in\{0,\ldots,M\}$. Here we applied a truncation procedure of the infinite phononic Hilbert space,[27,28] restricting ourselves to states with at most M phonons, i.e., $\Sigma_{\beta=1}^{G}m_{\beta}^{s}\leqslant M$. We carefully checked for the convergence of both the ground-state energy $E_0^{(M)}$ and the phonon distribution $C_{\beta}^{(M)}(m)$ as functions of M.

In the numerical work the matrix representation of $\mathcal{H}$ (as well as the vector representation of $|\psi\rangle$) requires a mapping of each index pair (r,s) on a single consecutive index, e.g., i. Particularly with regard to an implementation on parallel supercomputers, the following bijective mapping, $(r,s)\mapsto i$: $\{1,\ldots,D_{\mathrm{el}}\}\times\{1,\ldots,D_{\mathrm{ph}}^{(M)}\}\rightarrow\mu\{1,\ldots,D_{\mathrm{tot}}\}$, turned out to be advantageous:

$$\mu(r,s)=(r-1)D_{\mathrm{ph}}^{(M)}+s \tag{A4}$$

$$\mu^{-1}(i)=\left(\left\lfloor\frac{i-1}{D_{\mathrm{ph}}}\right\rfloor+1,i-\left\lfloor\frac{i-1}{D_{\mathrm{ph}}^{(M)}}\right\rfloor D_{\mathrm{ph}}^{(M)}\right), \tag{A5}$$

where $\lfloor x\rfloor$ is the largest integer $L\in\mathbf{N}$ with $L\leqslant x$.

Diagonalizing the PHM in a subspace with fixed electron numbers $N_{\uparrow}=N_{\downarrow}=\frac{3}{4}N$, a typical total dimension D_{tot} with which we dealt is 7 848 624 ($N=8$, $M=140$, and $G=2$). Despite the extreme sparsity of the matrices, the computation of the, e.g., 20 lowest eigenstates is still a numerical challenge: a typical production run for the parameters quoted above took about 30 minutes running on 64 processors of a CRAY T3E supercomputer.

APPENDIX B: JACOBI-DAVIDSON ALGORITHM WITH PRECONDITIONING

Many problems in theoretical physics are related to eigenvalue problems involving large sparse Hermitian matrices. To solve the eigenvalue problem numerically, iterative subspace methods like the Lanczos algorithm[29] or the Davidson algorithm[30] are commonly used to calculate the ground state and some excited eigenstates. However, these methods show a poor convergence and stability if the eigenvalues to be computed are not well separated or even degenerate. In that case, more sophisticated methods like the Jacobi-Davidson (JD) algorithm with preconditioning techniques[31,32] have to be used, providing both high resolution and rapid convergence.

The JD solvers use a succession of subspaces where the update of the subspace exploits approximate inverses of the problem matrix A. For A, $A=A^{H}$ or $A^{*}=A^{T}$ holds, where A^{*} denotes A with complex conjugate elements and $A^{H}=(A^{T})^{*}$ (transposed and complex conjugate).

The basic idea is: Let $\mathbf{V}^{k}$ be a subspace of $\mathbf{R}^{n}$ with an orthonormal basis $w_1^k,\ldots,w_m^k$, W a matrix with columns w_j^k, $S:=W^{H}AW$, $\overline{\lambda}_j^k$ eigenvalues of S, and T a matrix with the eigenvectors of S as columns. The columns x_j^k of WT are approximations of eigenvectors of A with Ritz values $\overline{\lambda}_j^k=(x_j^k)^{H}Ax_j^k$ that approximate eigenvalues of A. Let us assume that $\overline{\lambda}_{j_s}^k,\ldots,\overline{\lambda}_{j_{s+l-1}}^k\in[\lambda_{\mathrm{lower}},\lambda_{\mathrm{upper}}]$. For $j\in j_s,\ldots,j_{s+l-1}$, define

$$q_j^k=(A-\overline{\lambda}_j^k I)x_j^k,\quad r_j^k=(\overline{A}-\overline{\lambda}_j^k I)^{-1}q_j^k, \tag{B1}$$

and $\mathbf{V}^{k+1}=\mathrm{span}(\mathbf{V}^k \cup r^k_{j_s} \cup \cdots \cup r^k_{j_{s+l-1}})$ where $\overline{A}$ is an easy to invert approximation to A [$\overline{A}=\mathrm{diag}(A)$ in Ref. 33]. Then $\mathbf{V}^{k+1}$ is an $(m+l)$-dimensional subspace of $\mathbf{R}^n$, and the repetition of the procedure above gives in general improved approximations to eigenvalues and eigenvectors. Restarting may increase efficiency. Convergence is reached for the eigenvalue k, if the residual norm $\sqrt{\Sigma^n_{j=1}(r^k_j)^2}$ falls below an initial residual norm (calculated from the first eigenvector approximation) times a convergence factor ε.

For good convergence, $\mathbf{V}^k$ has to contain crude approximations to all eigenvectors of A with eigenvalues smaller than λ_{lower}.[33] The approximate inverse must not be too accurate, otherwise the method stalls. The reason for this was investigated in Ref. 31, and leads to the JD method with an improved definition of r^k_j:

$$\{[(I-x^k_j)(x^k_j)^H](\overline{A}-\overline{\lambda}^k_j I)[I-x^k_j(x^k_j)^H]\}r^k_j=q^k_j. \quad \text{(B2)}$$

The projection $[I-x^k_j(x^k_j)^H]$ in Eq. (B2) is not easy to incorporate into the matrix, but there is no need to do so, and solving Eq. (B2) is only slightly more expensive than solving Eq. (B1). The method converges quadratically for $\overline{A}=A$.

The character of the JD method is determined by the approximation $\overline{A}$ to A. For obtaining an approximate solution of the preconditioning system [Eq. (B2)], we may try an iterative approach.[31,34,35] In this work, a real symmetric version of the so called *quasi minimal residual* algorithm was used that is directly applied to the projected system [Eq. (B2)] with $\overline{A}=A$. By controlling the quasi-minimal residue norms we can adapt the accuracy of solving Eq. (B2) to the accuracy of the JD steps.

To illustrate the advantage of the JD algorithm as compared with the standard Lanczos technique, we have calculated the lowest 30 eigenvalues of a Hamilton matrix with total dimension $D_{\mathrm{tot}}=263\,536$, comparing both methods. For this comparison, we used a double-mode approach applying the following model parameters: $N=4$, $M=180$, $\Delta=1.2$, $U_{\mathrm{Cl}}=0$, $U_{\mathrm{Pt}}=0.8$, $\lambda_R=0.2$, $\hbar\omega_R=0.05$, $\lambda_{\mathrm{IR1}}=0$, and $\hbar\omega_{\mathrm{IR1}}=0.06$. The convergence factor ε was set to 10^{-7}.

Calculating the lowest 30 eigenvalues, the maximum size of the Jacobi-Davidson subspace was set to 100, triggering a restart of the whole process with the last approximations whenever the subspace size reached that value. The Lanczos process was stopped under the condition that the 30th eigenvalue converged within an accuracy ε. Due to implementation reasons, the Lanczos version of our diagonalization routine compared the difference between two succeeding eigenvalue approximations to check convergence. The results are shown in Fig. 18.

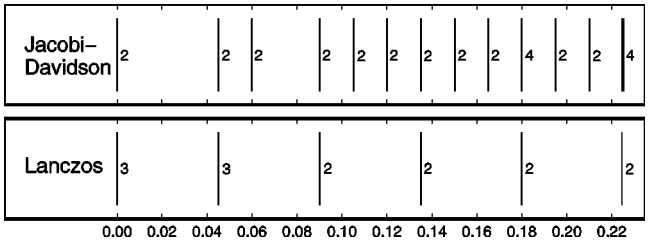

FIG. 18. Low-energy part of the eigenvalue spectrum of a high-dimensional Hamiltonian matrix as determined by the JD and Lanczos algorithms (for further explanation, see the text). The numbers to the right of the bars give the degeneracy of the corresponding eigenvalue.

The efficiency of the JD method is determined by the performance of the matrix-vector multiplication, which depends heavily on the storage scheme used. The extreme sparsity of the matrices used in this work ($\sim$10 nonzero elements per row, and matrix dimension up to 10^8) calls for a solution where only the nonzero elements are stored. To achieve high performance on all modern supercomputer architectures, a so-called *jagged diagonal* storage scheme[36] was implemented, which makes no assumptions about the sparsity structure of the matrix. A detailed description of the implementation on various massively parallel and vector supercomputers was presented in Ref. 36, together with a performance analysis.

As a conclusion, from a comparison between Lanczos and Jacobi-Davidson methods we can state that Lanczos is the appropriate choice for calculating few nondegenerate extreme eigenvalues. The growth of the Lanczos subspace limits the number of eigenvalue approximations that can be computed within a reasonable amount of time. For the Jacobi-Davidson method, the maximum subspace size can be limited by the user as a restarting technique is applied. So this algorithm is used for computing many eigenvalues with high resolution.

For performance reasons, our Jacobi-Davidson implementation stores the nonzero matrix values only. The price for this achievement are the relatively high memory costs which limit the size of computable problems. Our Lanczos implementation creates matrix elements during the runtime, which enables us to handle much larger problems with this routine.

[1] D. Baeriswyl and A.R. Bishop, Phys. Scr. **T19**, 239 (1987); J. Phys. C **21**, 339 (1988).

[2] J.T. Gammel, A. Saxena, I. Batistić, A.R. Bishop, and S.R. Phillpot, Phys. Rev. B **45**, 6408 (1992); S.M. Weber-Milbrodt, J.T. Gammel, A.R. Bishop, and E.Y. Loh, Jr., *ibid.* **45**, 6435 (1992).

[3] S.P. Love, L.A. Worl, R.J. Donohoe, S.C. Hucket, and B.I. Swanson, Phys. Rev. B **46**, 813 (1992).

[4] S.P. Love, S.C. Huckett, L.A. Worl, T.M. Frankcom, S.A. Ekberg, and B.I. Swanson, Phys. Rev. B **47**, 11 107 (1993).

[5] X.Z. Huang and A.R. Bishop, Phys. Rev. B **48**, 16 148 (1993).

[6] The general stoichiometric compound can be represented by $[M^{\rho-\delta}L_2][M^{\rho+\delta}X_2L_2]Y_4$ $(0<\delta<1)$ for CDW materials and $[ML_2X]Y_2$ for SDW MX materials, where L is a ligand and Y is a counterion.

[7] A.S. Dolgov Fiz. Tverd. Tela (Leningrad) **28**, 1641 (1986) [Sov. Phys. Solid State **28**, 907 (1986)]; A.J. Sievers and S. Takeno, Phys. Rev. Lett. **61**, 970 (1988); J.B. Page, Phys. Rev. B **41**, 7835 (1990).

[8] B.I. Swanson, J.A. Brozik, S.P. Love, A.P. Shreve, A.R. Bishop, W.-Z. Wang, and M.I. Salkola, Phys. Rev. Lett. **82**, 3288 (1999).

[9] H. Fehske, G. Wellein, H. Büttner, A.R. Bishop, and M.I. Salkola, Physica B **281&282**, 673 (2000).

[10] Since the ILM's are rather localized phonon excitations, a finite-cluster diagonalization of even such a small system will give trustworthy results.

[11] The frequently used single-band description (Ref. 1) is appropriate as long as the difference between the *M* and *X* atomic levels is sufficiently large.

[12] Longer-range Coulomb effects have been investigated (Refs. 2 and 5). Such extensions will not change our qualitative discussion.

[13] W.P. Su, J.R. Schrieffer, and A.J. Heeger, Phys. Rev. Lett. **42**, 16 698 (1979); Phys. Rev. B **22**, 2209 (1980); **28**, 1138(E) (1983).

[14] R.C. Albers, Synth. Met. **29**, F169 (1989); R.C. Albers, M. Alouani, J.M. Wills, and M. Springborg, **41-43**, 2739 (1991); M. Alouani, J.W. Wilkins, R.C. Albers, and J.M. Wills, Phys. Rev. Lett. **71**, 1415 (1993); *ibid.* **73**, 3599 (1994).

[15] M. Alouani, R.C. Albers, and J.M. Wills, Synth. Met. **55-57**, 3358 (1993); V.I. Anisimov, R.C. Albers, J.M. Wills, M. Alouani, and J.W. Wilkins, Phys. Rev. B **52**, R6975 (1995).

[16] M. Alouani, R.C. Albers, J.M. Wills, and J.W. Wilkins, Comput. Mater. Sci. **10**, 381 (1998).

[17] If we had used the very large values of the Pt *U* parameter obtained by means of the constrained LDA ($U_d^{(\mathrm{solid})} \sim 4-5$ eV; see Ref. 15), within our effective (eight-site) PHM description a strong-SDW ground-state would result.

[18] R.H. McKenzie and J.W. Williams, Phys. Rev. Lett. **69**, 1085 (1992).

[19] H. Fehske, M. Holicki, and A. Weiße, Adv. Solid State Phys. **40**, 235 (2000).

[20] E. Jeckelmann, C. Zhang, and S.R. White, Phys. Rev. **60**, 7950 (1999).

[21] Choosing the eight-site lattice has the main advantage that there are electronic levels at Fermi points located in the upper band at $K_F = \pm \pi/2$ (supposing a two-band charge transfer situation is realized). Then, in principle, an arbitrary small *U* or λ_R can break the degeneracy of these levels by opening a SDW or CDW gap. For the four- and 12-site lattices, finite-size effects prevent an accurate analysis of the gap formation (diagonalizing the 16-site PHM exceeds the capacities of the present-day supercomputers). A detailed analysis of finite-size effects in the PHM can be found in Ref. 22.

[22] M. Kinateder, Master's thesis, University of Bayreuth 2000 (unpublished).

[23] Note that L_i is a measure of the single occupancy of site *i*, varying, e.g., for the half-filled Hubbard model, from 3/4 (atomic limit; $U \to \infty$) to 3/8 (band limit; $U = 0$).

[24] B. Bäuml, G. Wellein, and H. Fehske, Phys. Rev. B **58**, 3663 (1998).

[25] Indeed, it was shown recently (Ref. 9), that the entire charge transfer Δ effect can be modeled dynamically by a strong coupling to the IR1-mode (DMA).

[26] Y. Wada, T. Mitani, K. Toriumi, and M. Yamashita, J. Phys. Soc. Jpn. **58**, 3013 (1989).

[27] Y. Inada and C. Ishii, J. Phys. Soc. Jpn. **59**, 612 (1990).

[28] G. Wellein, H. Röder, and H. Fehske, Phys. Rev. B **53**, 9666 (1996).

[29] J.K. Cullum and R.A. Willoughby, *Lanczos Algorithms for Large Symmetric Eigenvalue Computations*, (Birkhäuser, Boston, 1985).

[30] E.R. Davidson, J. Comput. Phys. **17**, 87 (1975).

[31] G.L.G. Sleipjen and H.A. van der Vorst, SIAM J. Matrix Anal. Appl. **17**, 401 (1996).

[32] A. Basermann and B. Steffen, *New Preconditioned Solvers for Large Sparse Eigenvalue Problems on Massively Parallel Computers*, Proceedings of the Eighth SIAM Conference on Parallel Processing for Scientific Computing, CD-ROM, SIAM (Philadelphia, 1997).

[33] N. Kosugi, J. Comput. Phys. **55**, 426 (1984).

[34] A. Basermann and B. Steffen, in *Parallel Computing: Fundamentals, Applications and New Directions*, edited by E.H. D'Hollander, G.R. Joubert, F.J. Peters, and U. Trottenberg, (Elsevier, Amsterdam, 1998).

[35] A. Basermann, in *Parallel Preconditioned Solvers for Large Sparse Hermitian Eigenvalue Problems*, edited by Jack Dongarra and Vicente Hernandez, VECPAR'98—Third International Conference for Vector and Parallel Processing, Lecture Notes in Computer Science (Springer, Berlin, 1999), Vol. 1573, pp. 72–85.

[36] M. Kinateder, G. Wellein, A. Basermann, and H. Fehske, in *High Performance Computing in Science and Engineering '00*, edited by E. Krause and W. Jäger, (Springer-Verlag, Berlin, 2001), pp. 188–204.